42nd AIAA/ASME/SAE/ASEE Joint Propulsion Conference
Sacramento, CA, July, 2006

AIAA-2006-4498

Discharge Hollow Cathode and Extraction Grid Analysis for the MiXI Ion Thruster

Richard Wirz*
Jet Propulsion Laboratory, California Institute of Technology, Pasadena, CA

Regina Sullivan+, JoHanna Przybylowski+, Mike Silva+
California Institute of Technology, Pasadena, CA

Abstract - *Miniature ion thrusters are well-suited future space missions such as Terrestrial Planet Finder – Interferometer (TPF-I), where high efficiency thrusters using non-contaminating noble gas propellant are desirable. Transient dynamic and orbital analyses have shown that the low-noise, continuous thrust of the Miniature Xenon Ion (MiXI) thruster is desirable for TPF-I formation rotation maneuvers when compared with other thruster options [1], [2]. The 3cm diameter MiXI thruster, Figure 1, was originally designed using experimental methods and is capable of high Isp (> 3,000 sec), propellant efficiency > 80%, and thrust from <0.1 mN to >1.5 mN [3]. The MiXI thruster must demonstrate high levels of thrust resolution and a low minimum impulse bit to ensure it meets the precision formation flying needs of missions such as TPF-I. A novel concept for controlling the ion extraction voltages yields the necessary thrust characteristics for the MiXI thruster. Experiments verify these techniques and two-dimensional computational models show that such techniques should have minimal effect on the lifetime of the thruster. During this effort, the MiXI thruster incorporates, for the first time, flight like hollow cathodes for both the discharge chamber and beam neutralization.*

Nomenclature

B = magnetic flux density

$D_{||}$ = parallel plasma diffusion coefficient

$D_{\perp}$ = perpendicular plasma diffusion coefficient

f_A = fraction of ion current to anode surfaces

f_B = fraction of ion current to the beam

f_C = fraction of ion current to cathode surfaces

F_B = beam flatness

J_B = total beam current

J_D = discharge current

J_i = current of ions created in discharge

J_{ip} = current of ions created in discharge by primaries

J_p = primary electron current

J_{screen} = screen grid ion current

$\dot{m}_d$ = discharge chamber propellant mass flow rate

n_e = secondary electron number density

n_i = ion number density (total)

n_o = neutral atom number density

(P_{ps}, P_{pw}, P_{piz}, P_{px}, P_{sw}, P_{siz}, P_{sx}) = electron power loss mechanisms (described in text)

r = distance from thruster axis

T_e = secondary electron temperature

T_i = ion temperature

T_p = primary electron temperature

T_o = neutral atom temperature

V_{accel} = accelerator grid voltage

V_B = beam voltage

V_D = discharge voltage

V_p = primary electron voltage

Greek Symbols

δ_D = plasma magnetization

δ_ν = electron collision ratio

ε_B = discharge loss

η_{ud} = discharge propellant utilization efficiency

Units:
This study uses mks units of the International System (SI) with the exception that energies are frequently given in terms of electron volts (eV).
sccm ≡ Standard Cubic Centimeters per Minute. For xenon: 1 sccm ≈ 0.09839 mg/s at STP.

eV/ion ≡ (Watts of Discharge Power)/(Amp of Beam Current) for discharge loss, ε_B

©2006 by the American Institute of Aeronautics and Astronautics, Inc. The U.S. Government has a royalty-free license to exercise all rights under the copyright claimed herein for Governmental purposes. All other rights are reserved by the copyright owner.
*Staff Engineer, Advanced Propulsion Technology Group

I. Introduction

A. Background and Motivation

Ion thrusters are well known for their ability to deliver continuous thrust at high efficiency (η_{tot} ~ 60-70%, η_{tot} ~80-90%) and high specific impulse (I_{sp} ~2,000-5,000 sec) with the use of benign propellants (e.g. xenon and argon). A miniature ion thruster that can provide these performance advantages at a maximum thrust near 3 mN and minimum thrust <0.1mN is attractive for a variety of future space missions.

Historically, miniaturization of ion thruster technologies has presented many design and performance challenges that have put the concept out of reach for mission designers. However, recent advancements have shown that reasonable performance is possible for small ion thruster if the development and validation of key technologies is continued. Previous studies on the Miniature Xenon Ion (MiXI) thruster (Figure figmixipic) have demonstrated an efficient discharge and ion extraction grid assembly using filament cathodes and the Internal Conduction (IC) cathode. The IC cathode demonstrated high performance but is a risky technology for ion thrusters due to its low maturity; therefore miniature hollow cathodes were designed and built specifically for the MiXI thruster.

Figure figmixipic. Miniature Xenon Ion (MiXI) thruster

The MiXI ion extraction grids have are designed to achieve a maximum thurst ~3.0 mN, and have thus far demonstrated high performance at nominal thrust levels. Previous to this study, the low thrust characteristics have not been investigated.

B. Objective

In Section II we use a combination of computational and experimental analysis to integrate and characterize MiXI's discharge hollow cathode. In Section III the MiXI grid is experimentally characterized in the low-thrust regime and the minimum thrust capability of the grids is determined. Some computational analysis of the grid behavior at low-thrust is also performed.

II. Discharge Hollow Cathode Integration

A. Miniature, Low-Flow Hollow Cathodes

Previous investigations show that attractive performance is possible for the MiXI thruster with low-power electron sources such as the hollow cathodes used in conventional ion thrusters. Hollow cathodes are a mature technology and typically require less power per amp of emitted electrons than other discharge cathode options. The use of conventionally-sized hollow cathodes presents a considerable efficiency challenge for miniature ion thrusters since they require a designated propellant feed (> 1 sccm) that can exceed the propellant needs for the entire MiXI discharge chamber (typically 0.1-0.5 sccm). Therefore, as discussed in Reference refwirzcath, using conventially-sized hollow cathodes for a miniature discharge may result in very low efficiencies and poor throttleability. However, the impressive performance of hollow cathodes may be realized for miniature ion thrusters if low-flow and low-power miniature hollow cathodes can be successfully designed, built, and implemented. As a result, two miniature hollow cathodes (Figure fighc) were designed and built specifically to operate at MiXI's low-flow and current conditions (typical discharge current, J_D, 50-500mA and beam current, J_B, ~ 10-20mA). These miniature hollow cathodes are sufficiently large to scale to larger ion thruster sizes (> 3

Figure fighc. MiXI's Miniature Hollow Cathodes

cm) and Hall thrusters, and may also provide a reliable and efficient option for neutralizing the plumes of other small electric propulsion thrusters.

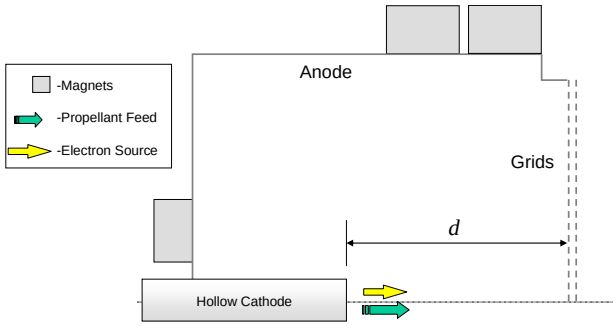

Figure figmixiconfig. Basic MiXI configuration showing axial distance, d, between cathode face and screen grid.

B. Discharge Hollow Cathode Location Analysis

JPL's ion thruster model (DC-ION) was used to simulate MiXI thruster performance at a range of axial locations of a miniature discharge hollow cathode. The axial location of the hollow cathode is referenced to the interior surface of the screen as shown in Figure figmixiconfig. The details of the DC-ION model and discharge hollow cathode simulations with DC-ION are given in References [refwirzjpc06, refwirzjpc05, refthesis]. The results from the analysis show (Figure figaxial) that an upstream location, similar to that of conventional ion thrusters, yields the best propellant efficiency and beam profile for nominal MiXI operation. Figure figprofiles shows that the beam profile is progressively peaked on-center as the hollow cathode is located closer to the extraction grids.

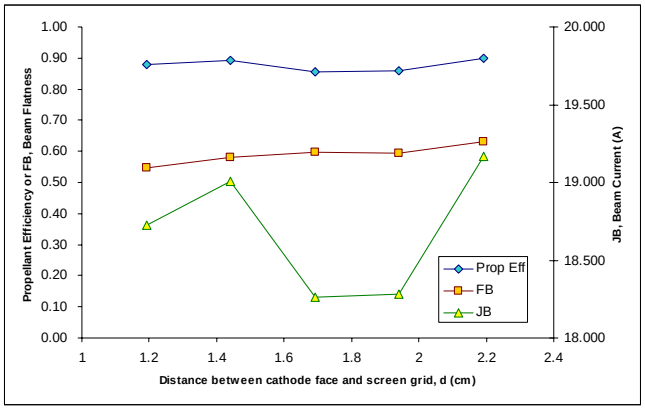

Figure figaxial. Anticipated MiXI thruster performance per axial location of hollow cathode face relative to screen grid. Default 3-ring MiXI configuration. Results generated by DC-ION model.

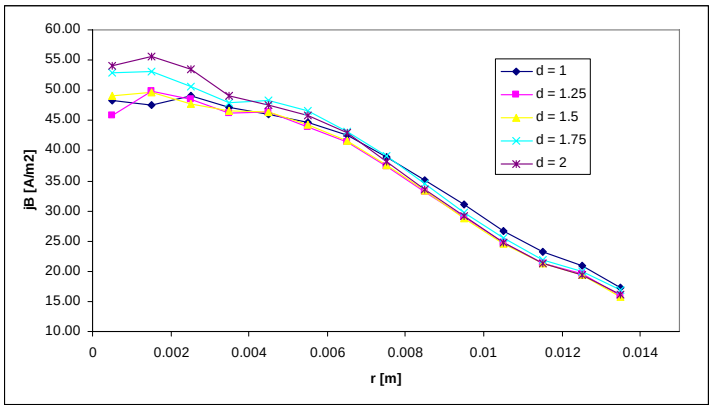

Figure figprofiles. Anticipated MiXI thruster beam profiles per axial location of hollow cathode face relative to screen grid. Results generated by DC-ION model.

C. Magnetic Field Analysis

Due to the small size of the MiXI discharge, there is some concern that the heat from the hollow cathode will demagnetize the cathode magnet, especially at more upstream cathode locations. To address this concern DC-ION also simulated the impact of changes to MiXI's magnetic field. Figure fignomag shows the impact on MiXI performance if the cathode magnet is almost completely removed (or demagnetized). If we assume that the cathode does not significantly heat the cathode magnet, then we can investigate if the performance is enhanced at higher cathode magnet strengths. Figure figcathmagdouble shows the expected performance if the cathode magnet strength is doubled from the MiXI baseline.

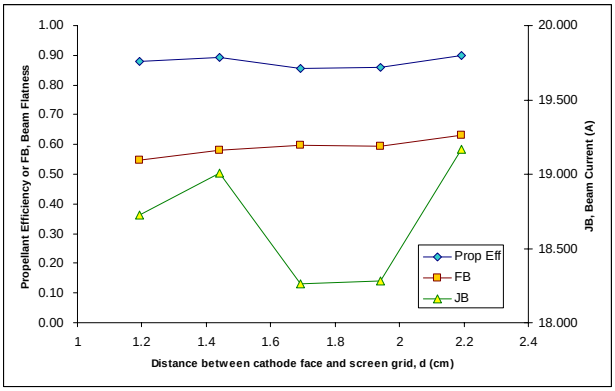

Figure figaxial. Anticipated MiXI thruster performance per axial location of hollow cathode face relative to screen grid. 2-ring MiXI configuration. Results generated by DC-ION model.

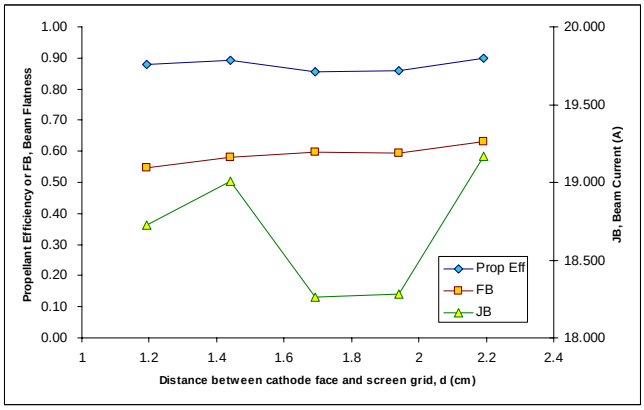

Figure figaxial. Anticipated MiXI thruster performance per axial location of hollow cathode face relative to screen grid. 3-ring MiXI configuration with double-strength cathode magnet. Results generated by DC-ION model.

D. Initial Hollow Cathode Testing

E. Discussion of Hollow Cathode Results

III. Low Thrust Analysis for Extraction Grids

The grid region of ion thrusters is a space-charge limited system. Space-charge limited systems arise when an electrical field is complicated by charged particle flow. Consider the linearly varying electric field between two parallel plates. If ions are transmitted across the plates, the field between the plates is modified. When there is a charge flux, the maximum current density that can be extracted through a distance L for a specified potential difference is given by the Child-Langmuir Law (Jahn, 1968):

$$j_{sc} = \frac{4\varepsilon_0}{9}\sqrt{\frac{2e}{m_i}}\left(\frac{V_T^{3/2}}{L}\right) \tag{1}$$

Where j_{sc} is the total current flux across the plates. In space-charge limited operation, the particle flux will increase until the maximum current is reached. Thus, the current density defined in Eq(1) can be considered the steady-state current, provided that the particle supply is not exhausted; for all other currents a transient state exists while the electrical and dynamical parameters balance. For example, if the current density is less, the ion flux will increase in response to the potential distribution.

In addition to this space-charge defined current density, there are physical limitations on the maximum beamlet current density. These are known as perveance limits and depend on the geometry of the grids. The definition of the perveance quantity is (Aston et al, 1978):

$$p = \frac{j_B}{V_T^{3/2}}, \tag{2}$$

This definition is based upon the current density of the beam, which is non-uniform across a beam profile due to a non-uniform ion density distribution in the discharge chamber. Thus, a more appropriate operational definition of perveance for a specific thruster is given by Eq(3), which is based upon the total beam current.

$$P = \frac{J_B}{V_T^{3/2}}, \tag{3}$$

Cartoons of the plasma sheath between the grids are shown in Figure 1. Figure 1a shows the nominal operating condition when there is no ion impingement on the accelerator grid. Figure 1b and c show the cases of cross-over impingement and direct impingement, respectively. The occurrence of impingement is the basis for the geometrical constraints on perveance. Impingement reduces thruster efficiency and results in degradation of the accelerator grid, which can substantially reduce the thruster lifetime. During nominal operation the beamlet current density is the current density defined in the Child-Langmuir Law ($j_B = j_{sc}$).

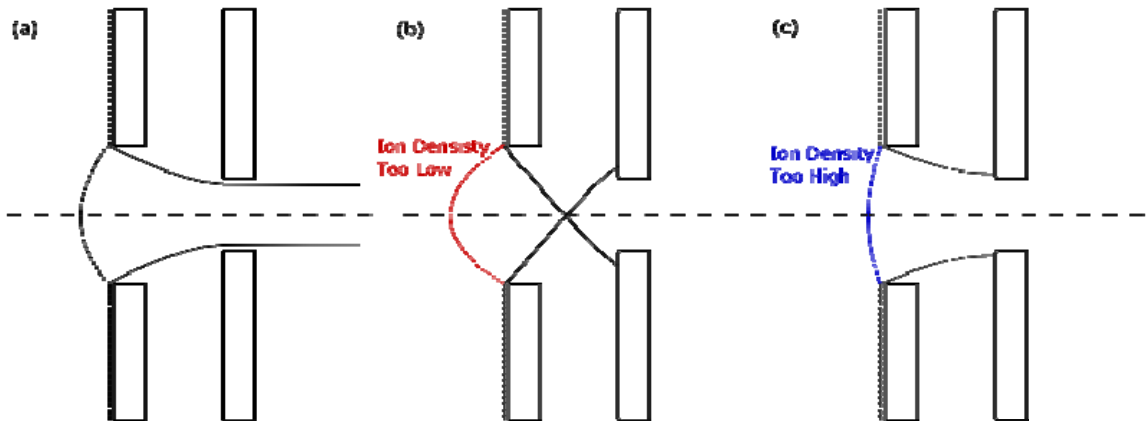

Figure 1 – Plasma Sheaths in the Grid Region: (a) Nominal, (b) Cross-Over Impingement, (c) Direct Impingement

The upper and lower perveance limits are functions of grid geometry and the discharge chamber ion density.

$$P = \frac{J_B}{V_T^{3/2}} = f(n_i, geometry) \tag{4}$$

For a given geometry, in order to preserve the space-charge-defined current density through the screen grid, j_{sc}, lower ion densities correspond to larger sheath surface areas, and higher ion densities correspond to smaller sheath surface areas. Thus, when n_i is too low, cross-over impingement occurs; and when n_i is too high, direct impingement occurs. The sheath surface is an equipotential line of the electric field.

A. MiXI's High-Performance Extraction Grids

Early test showed the advantages of SHAG optics for the MiXI scale. Computational analysis was used to design MiXI grids that exhibit high-performance by incorporating high ion transparency and low neutral transparency. The current MiXI grid set, shown in Figure figgrids, also exhibits long grid life and low susceptibility to thermal deflections compared to earlier designs. The maximum thrust capacity (assuming a beam flatness of only 0.6) with the current MiXI grid set is ~3mN. In this analysis we investigate the lower thrust limit of the MiXI grid set by examining the direct impingement limits with computational and experimental analysis. For this investigation, MiXI-II uses filament cathodes for the neutralizer (shown in Figure figmixi2pic) and discharge electron source.

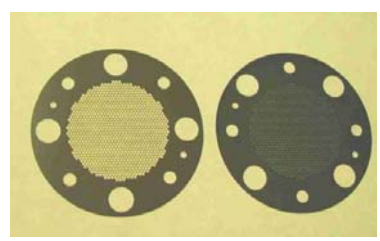

Figure figgrids. MiXI's high-performance grids

B. Experimental Testing Apparatus

The Second Miniature Xenon Ion Thruster (MiXI-II)

Regina Sullivan built a second lab model of the 3cm diameter MiXI thruster, MiXI-II, for characterization of MiXI components, performance, and beam. The thruster, shown in Figure figmixi2pic, was also built to serve as a high-purity, highly-controllable beam source for characterizing beam diagnostics. The low-flow rate (<1 sccm) and high propellant efficiency capability (~80%) of MiXI minimizing the ratio of background gas to charged beam components. MiXI also provides a low content of double ions and fine control of thrust level and divergence angle. Figure figmixi2 shows MiXI-II mounted in the vacuum chamber using the high-performance grids developed in previous investigations.

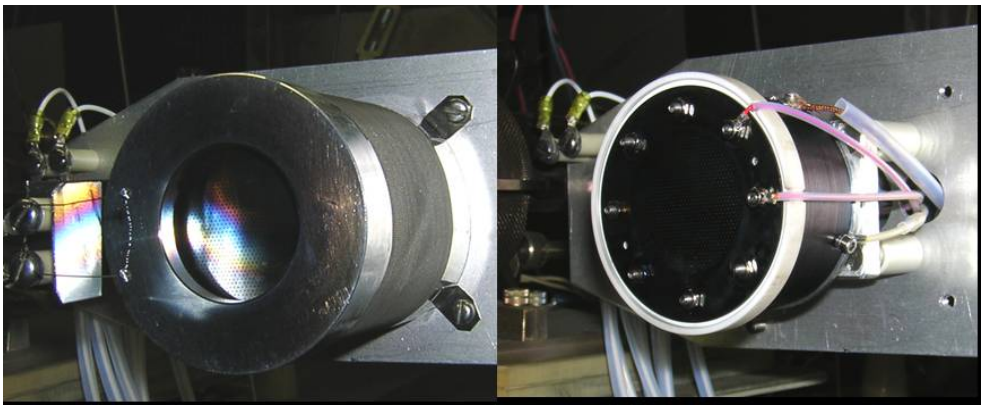

Figure figmixi2pic – Photograph of the MiXI-II thruster with plasma screen (left) and without its outer plasma screen (right).

Power and Thruster Diagnostics

The MiXI thruster requires 5 power supplies for operation. The basic circuit diagram for the thruster is shown in Figure .

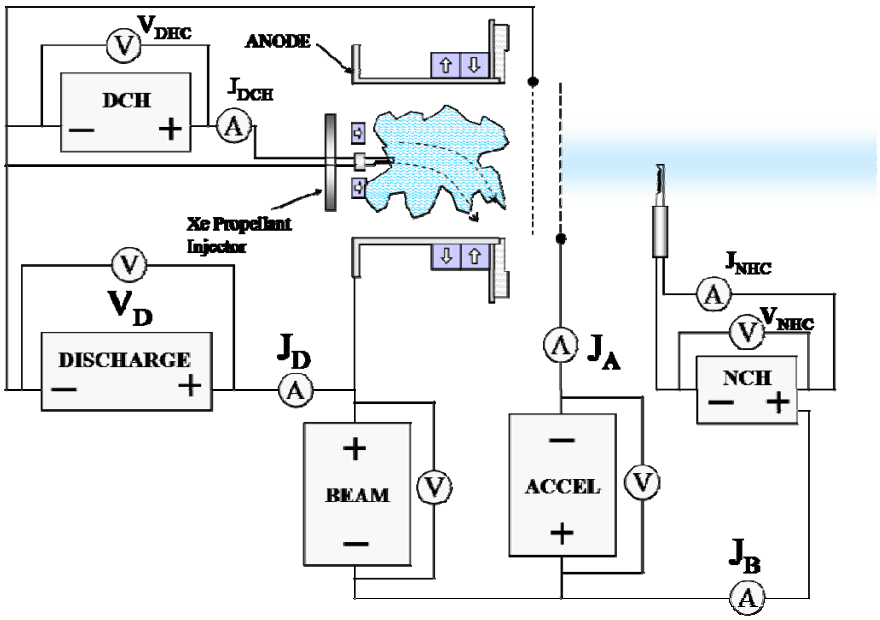

Figure figmixi2diag – Circuit diagram for MiXI-II thruster

The data acquisition system for MiXI-II consists of 11 digital multi-meters and a digital thermometer, which measured the parameters listed in Table tabparam.

Table tabparam – List of experimental parameters

Parameter	Description
V_{DCH}	Voltage across discharge cathode heater
J_{DCH}	Current through discharge cathode
V_D	Voltage between negative side of discharge cathode and anode wall

J_D	Current from discharge cathode to anode wall, through the discharge plasma
V_B	Voltage between thruster body and ground potential
J_B	Electron current required to neutralize the beam (equal in magnitude to the ion current in the beam)
V_A	Voltage between "accel" grid and ground potential
J_A	Current to "accel" grid ("impingement" current)
V_{NCH}	Voltage across neutralizer cathode heater
J_{NCH}	Current through neutralizer cathode
V_F	Voltage of thruster ground potential relative to earth ground
T	Temperature of thruster body

Vacuum Facility

The facility in which the experiment was conducted was the 2m diameter vacuum chamber in Building 149 of the Jet Propulsion Laboratory, also known as "Big Green" (see Figure). Initially, the plan was to use another vacuum chamber at JPL. Although numerous modifications were made to this chamber, it was not possible to achieve the desired vacuum pressure, so the experiment was moved to "Big Green."

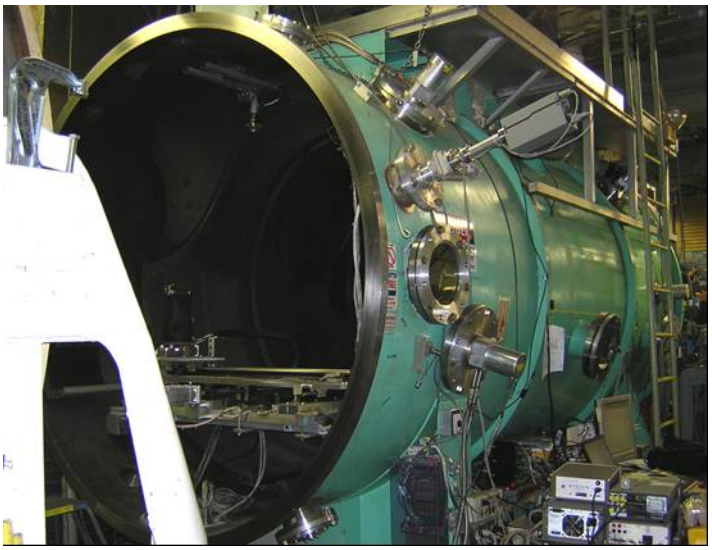

Figure figgreen – "Big Green" vacuum chamber

"Big Green" is outfitted with 3 diffusion pumps and 2 cryo-pumps, as well as several mechanical pumps. In these experiments, only the diffusion pumps were used. The vacuum achievable with these pumps was between $1x10^{-6}$ and $5x10^{-6}$ torr depending on propellant flow rate, which was more than satisfactory for the purposes of the experiment. The MiXI thruster was pointed towards the back of the chamber, and was offset 6.3 inches from the centerline of the chamber to allow room for a Hall thruster mounted on the same side of the chamber.

C. Experimental Analysis of Low Thrust Regime

Experimental Technique

During each test case of the experiment, the discharge current, J_D, was set at a specific value while the total accelerating voltage between the two grids, V_B-V_A or V_T, was varied. This was meant to simulate a steady discharge with a constant ion density. In reality, J_D was not completely constant; it decreased slightly as the beam current, J_B, was increased, due to the removal of ions from the discharge chamber. (The reason why J_{DCH} and V_D were not continually adjusted to keep J_D constant was that the power supply controls were not sensitive enough.) So it is useful to view the data sets obtained in the experiment primarily as a function of net accelerating voltage, but to keep in mind the influence of J_D. A list of the different cases tested in the experiment can be found in Table 1.

Table 1 – List of experimental test cases

Test Case	Initial J_D [mA]	V_{TOT} range [V]	Flow rate [sccm]
051606_1	151	200-900	0.5
051606_2	74	200-900	0.5
051606_3	41	200-1050	0.5
051606_4	21	200-1050	0.5
051806_1	65	200-1000	0.5
051806_2	51	200-950	0.6
051906_1	67	200-900	0.5
051906_2	77	200-900	0.6
051906_3	40	200-1050	0.6
051906_4	25	200-1000	0.6
052306_1	13	10-1000	0.5

For each case, after a discharge was established and a beam initiated, the voltage on the "screen" grid was increased. Typically, the voltage was increased in increments of 50 V. Each time the voltage was increased the values of the parameters listed in Table were recorded. The most important of these parameters were J_D, J_B, and J_A, which changed as V_B was increased.

Beam Focusing Experimental Results

Beam current and accel grid current data were obtained for each test case listed in Table 1. As previously mentioned, for each test case J_D was set at an initial value, and then the total accelerating voltage, V_T, was increased.

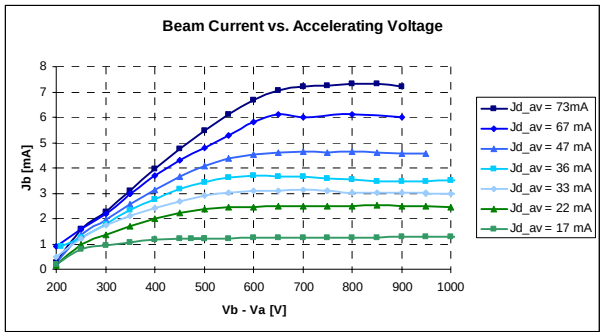

Figure 2 shows a representative collection of J_B values for the different test cases, while Figure 3 shows a representative collection of J_A values for the different test cases.

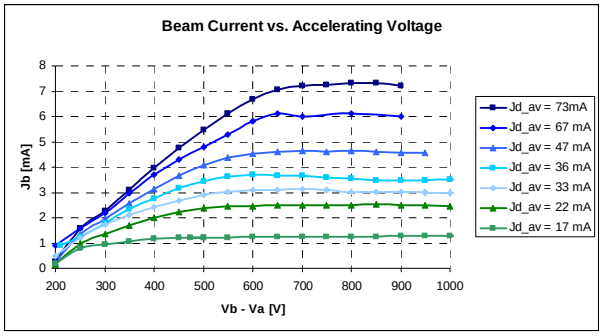

Figure 2 – Summary of Beam Current Data

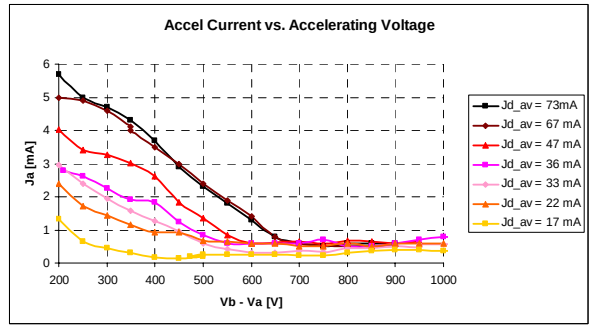

Figure 3 – Summary of Accel Grid Data

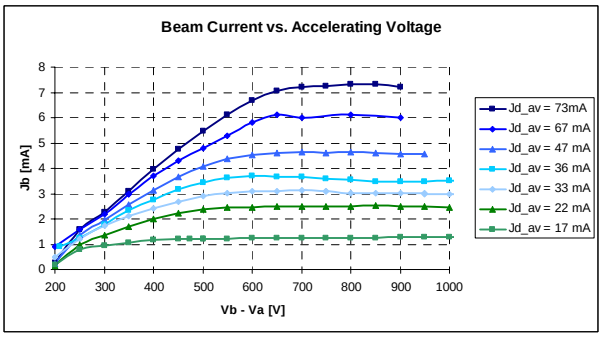

Figure 2 shows that for each case, as the total voltage is increased above a certain value J_B becomes relatively constant. Additionally, it shows that as J_D decreases, the voltage at which J_B become constant decreases.

Figure 3 shows that as the accelerating voltage is increased above a certain value J_A becomes relatively constant. Additionally, it shows that as J_D decreases, the voltage at which J_A become constant decreases.

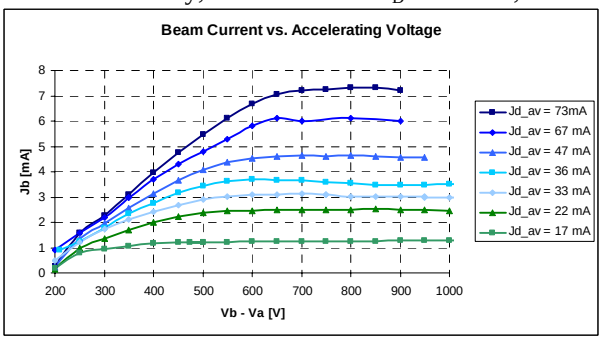

Figure 2 and Figure 3 indicate an inverse relationship between J_A and J_B. As J_B reaches a constant maximum value, J_A reaches a constant minimum value. This relationship can be seen more clearly in Figure 4.

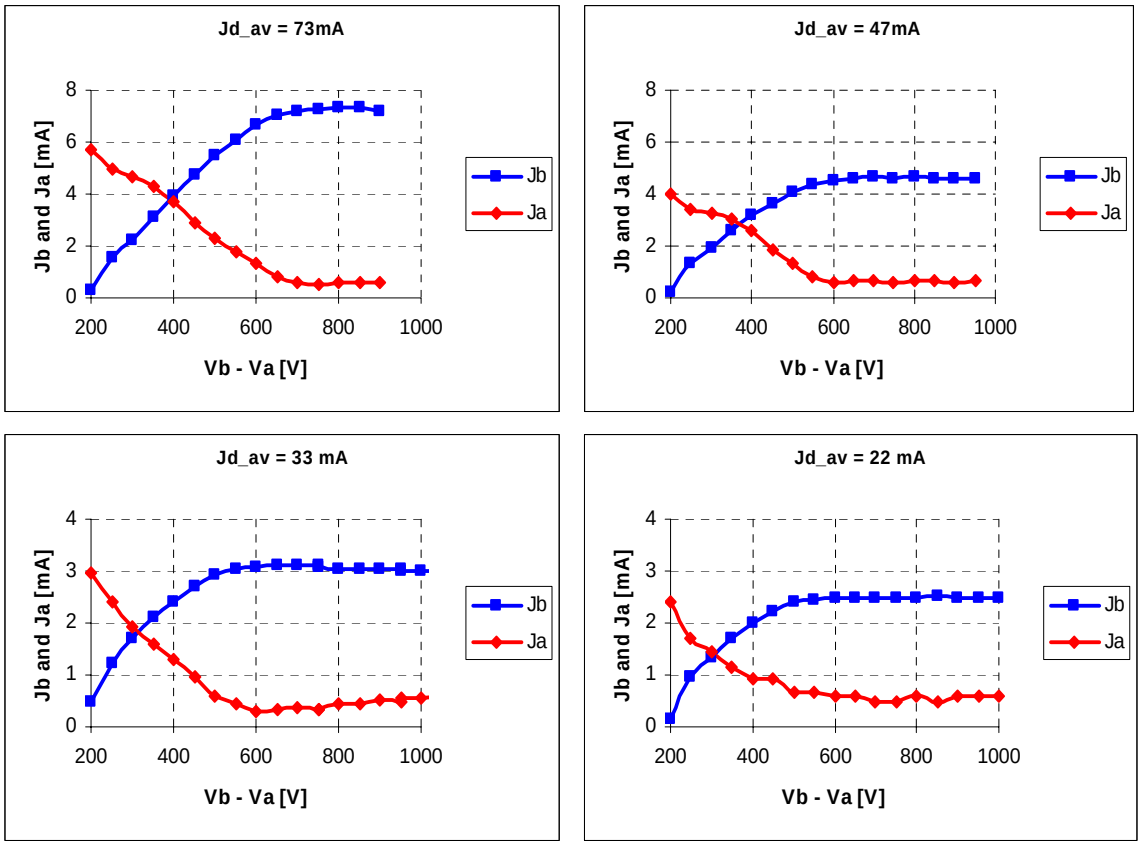

Figure 4 – J_B and J_A data for various average values of J_D

From these graphs it is clear that for a given J_D, the currents J_B and J_A reach constant values at approximately the same accelerating voltage. For an average J_D of 73 mA, this voltage occurs at about 700 V; for an average J_D of 47 mA, this voltage occurs at about 600 V; for an average J_D of 33 mA this voltage occurs at about 600V, and for an average J_D of 22 mA, this voltage occurs at about 500 V. This data thus shows a general trend: as J_D decreases, the accelerating voltage required to obtain constant values of J_A and J_B decreases.

Figure 4 also suggests that the voltage at which the J_B and J_A cross generally increases as J_D increases. This can also be seen (perhaps more clearly) in a 3D plot of the data, with the variables V_T-, J_D, and J_B or J_A on the three axes. Figure 5 shows two different perspectives of this 3D plot, with J_B and J_A represented in 3D by the two different surfaces.

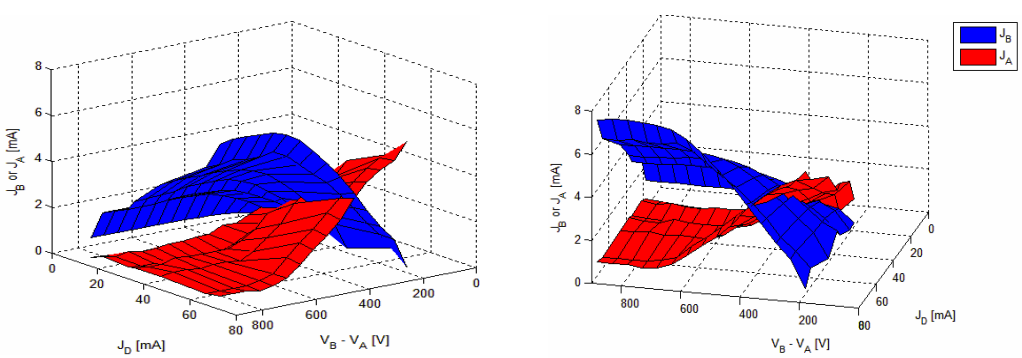

Figure 5 – 3D Plot of the experimental data (2 perspectives)

The bottom view in Figure 5 indicates that as J_D increases, the points of intersection between the two surfaces tend towards higher values of V_T; this relationship is also seen in the theoretical results produced by the model.

This experiment was primarily aimed at the low discharge current regime. Potential missions considering the MiXI thruster, such as JPL's Terrestrial Planet Finder mission, require MiXI to produce thrust values that fall at the low end of its operational spectrum. Therefore, test cases were conducted with the discharge current as low as physically possible (i.e. less than 20 mA). Two test cases at low discharges are shown in Figure 6. Both of these graphs show trends consistent with those seen in Figure 4. For an average J_D of 17 mA, the voltage at which J_A and J_B become approximately constant occurs at around 400 to 450 V. For the 13 mA case, this appears to occur at around 450 to 500 V, although it is difficult to tell the exact point due to the fluctuations in the curves (especially the J_A curve). It should be noted that the low J_D test cases seem to exhibit greater fluctuations in J_B and J_A than those conducted at higher values of J_D.

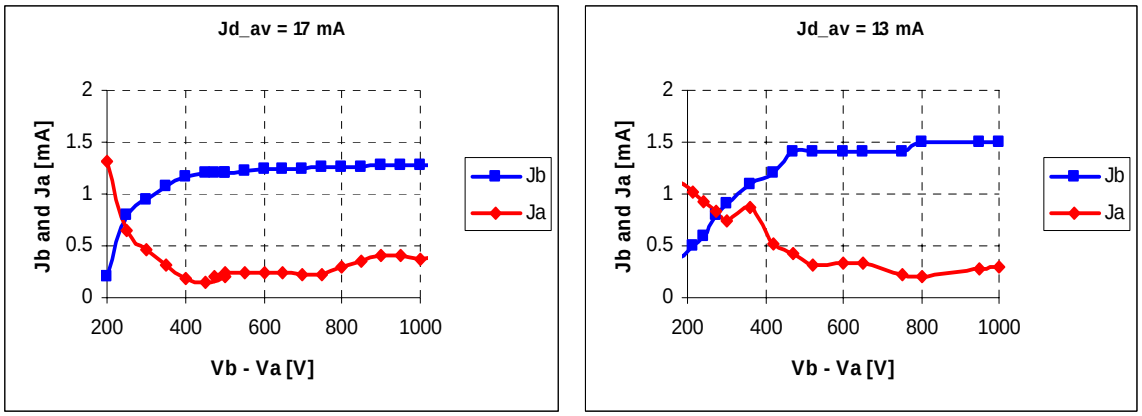

Figure 6 – J_B and J_A data for low average J_D values

C. Computational Analysis of Low Thrust Regime

Computational Model of Grid Optics, CEX2D

Simulations of the MiXI thruster operation were performed using a 2-D ion optics code developed at JPL. The computer code, known as CEX2D, models a single pair of screen and accelerator grid apertures. The code is capable of modeling many aspects of ion thruster performance including perveance, electron backstreaming, and accelerator grid hole wall erosion rate. The values extracted from the code were beamlet current and current to the accel grid as beam voltage and ion density in the discharge chamber were varied. The rest of the parameters, accel voltage, discharge voltage, and grid geometry were held constant at the same values implemented experimentally. Varying the beam voltage for a given ion density matches the actual experiment as discharge current and ion density are closely related. The ion density parameter used in the code can be recast in terms of the discharge current found experimentally with more knowledge of the discharge process. The ion density to discharge current relation may also be determined by matching the measured beam current and beam voltage to the code output.

Computational Results

Under proper conditions the beamlet is focused through the grids as can be seen in Figure 7. The trajectories of several ions are plotted and the direct impingement on the accel grid is removed when the beamlet is focused.

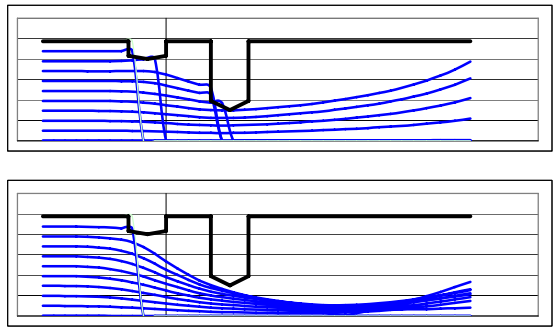

Figure 7 – Example of beam focusing for Vb-Va = 250V (top) and for Vb-Va = 550V (bottom).

The output from the CEX2D code is shown in Figure 8 for a large parameter space where beam and accel grid currents are plotted verses the beam voltage and ion density. A number of interesting aspects can be drawn from the figure. First, the characteristic of beam focusing can be seen that for a given ion density increasing the beam voltage leads to an increase in beam current and a decrease in accel current. At some beam voltage the accel current goes to zero, the beam current reaches a constant value and thus the beam is focused.

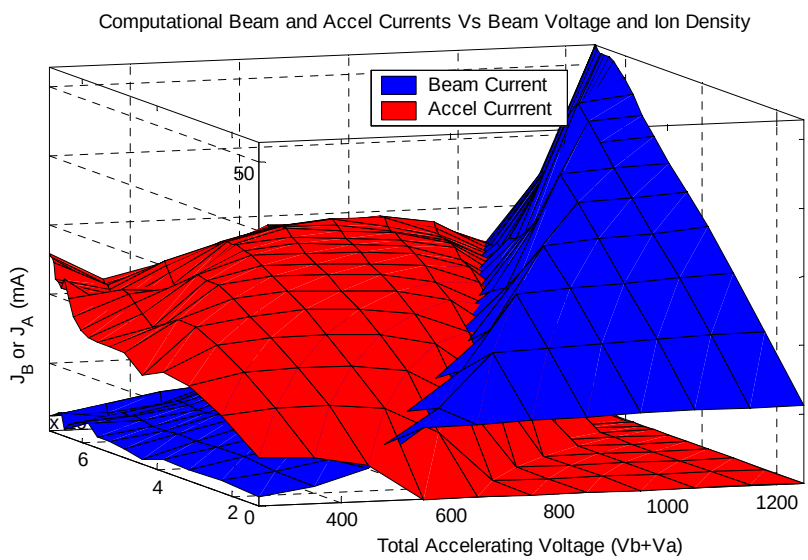

Figure 8 – Computational MiXI Operational Space

D. Discussion of low-thrust analysis of extraction grids

Discussion of Experimental Results

In most of the tests, it was possible to determine the point at which the grids were fully focused. If the potential between the grids is lower than that required for complete focusing, some direct impingement of the ions on the accel grid will occur. As the potential is increased, the ion beamlets become more focused, and thus the ion current to the accel grid (J_A) decreases. In the experiment focusing could be seen as a decrease in J_A and an increase in J_B. The grids were deemed completely focused when J_A and J_B reached constant values. Even after this was achieved, V_B was increased further until the beam became unstable. This instability was likely due to arcing between the grids due to the high potential between them. The test

was halted after either instability occurred or the temperature reached the "magnet burnout" point of 300 degrees C. (SmCo magnets start to lose strength if heated beyond 300 degrees). The purpose of further increasing V_B was to determine under what conditions cross-over impingement became evident. However, this point was never reached in the experiment because it occurred at a grid potential that was higher than could be physically achieved without arcing occurring between the grids.

Several results can be drawn from the results in the experimental data section. First of all, for every test case, J_B and J_A tended to an approximately constant value as V_T was increased above a certain value. This indicates that the lower focusing limit (i.e. the value of V_T at which ions are no longer directly hitting the accel grid) was reached. Thus, the experiment has characterized the lower focusing limit for a variety of thruster discharge conditions. Figure 2, Figure 3, and Figure 5, for example, could be used if one wanted to operate the thruster at a certain discharge current and needed to know the lowest value of V_T for which complete focusing could still be achieved.

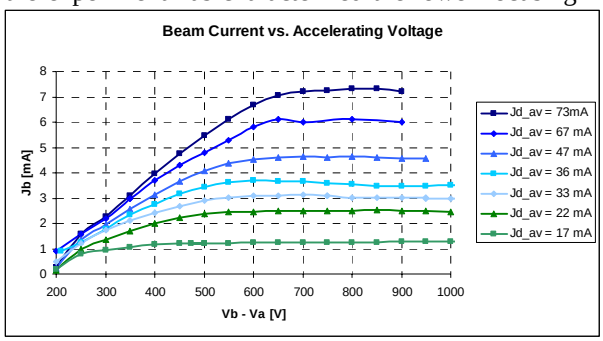

Comparison of Laboratory Results to Computational Results

The computational results produce trends similar to those found in the measured data. For example, 3-D plots of beam currents verses ion density and accelerating voltage produce cross over voltages that are qualitatively similar and max beam currents that are numerically similar to the measured data. The discrepancy between the computational and measured data is in the transition region where the beamlets are focusing. In Figure 9, the transition to focusing occurs more sharply in the computational data. This is most likely due to the simplifying assumption that the one beamlet represents the whole beam in an average sense. In reality, there is variation in the ion density in the discharge chamber and this leads to a variation in focusing voltage across the grid surface. Thus the transition to focused operation should be more gradual as seen in the measured data.

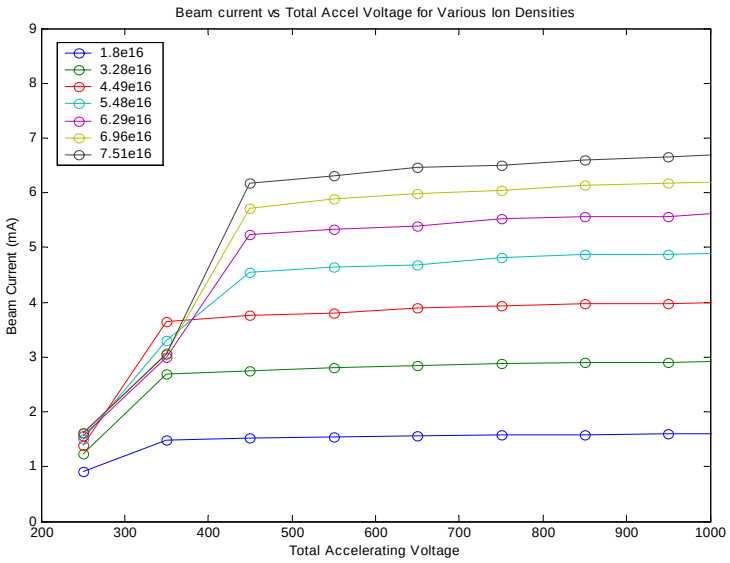

Figure 9 – Beam Current verses Accelerating Voltage

Also, the prediction of zero accel current is not realized in the measured data. After focusing occurs, there appears to be a nominal accel current of approximately 0.3 mA in the measured data. This could also be an effect of non-uniform ion density not focusing some beamlets as well as a small amount of ion impingement on the accel grid even after focusing. With the current assumptions, the computational model under predicts the focusing voltage and over predicts the rate at which the beam focuses. It can quite accurately predict the total beam current provided the correct flatness parameter is utilized.

VI. Conclusions

Acknowledgments

The research described in this paper was carried out by the Jet Propulsion Laboratory, California Institute of Technology, under a contract with the National Aeronautics and Space Administration in support of Project Prometheus.

References

[1] – Wirz R., "Discharge Plasma Processes of Ring-Cusp Ion Thrusters," Ph.D. Dissertation, Aeronautics, Caltech, Pasadena, CA, 2005

[2] – Wirz R., Polk J., Marrese C., Mueller J., "Development and Testing of a 3cm Electron Bombardment Micro-Ion Thruster," IEPC Paper 01-343, 27th IEPC, Pasadena, CA, Oct 2001

[3] – Wirz R., Polk J., Marrese C., Mueller J., "Experimental and Computational Investigation of the Performance of a Micro-Ion Thruster," AIAA-2002-3835, 38th JPC, Indianapolis, IN, July 2002

[4] – Wirz R., Mueller J., Gale M., Marrese C., "Miniature Ion Engine for Precision Formation Flying," AIAA-2004-4115, 40th Joint Propulsion Conference, Ft. Lauderdale, FL, 2004

[5] – Wirz R., Katz I., "Plasma Processes of DC Ion Thruster Discharge Chambers," AIAA Paper 2005-3690, 41st AIAA Joint Propulsion Conference, Tucson, AZ, 2005.

[1] - Li Y., Hamlin L., Wirz R., Adams D., Moore G., Coppolino R., Peng C., Levine M., "Dynamic Simulations for the Terrestrial Planet Finder Interferometer," Space Systems Optomechanics and Dynamics II, SPIE Conference, San Diego, August 2005 (to be published)

[2] - Wirz R., Mueller J., Marrese C., Gale M., "Miniature Ion Thrusters for Precision Formation Flying," AIAA-2004-4115, 40th JPC, Ft. Lauderdale, FL, July 2004

[3] - Wirz R., Polk J., Mueller J., Marrese C., Escobedo J., Sheehan P., "Development and Testing of a 3cm Electron Bombardment Micro-Ion Thruster," IEPC Paper 01-343, 27th IEPC, Pasadena, CA, Oct 2001